Carbonates Evaporites (2018) 33:255–274
https://doi.org/10.1007/s13146-017-0339-4

ORIGINAL ARTICLE

Evaporite mineral mapping and determining their source rocks using remote sensing data in Sirjan playa, Kerman, Iran

Azam Soltaninejad[1] · Hojjatollah Ranjbar[2] · Mehdi Honarmand[3] · Sara Dargahi[4]

Accepted: 31 January 2017 / Published online: 13 February 2017

Abstract In this research, evaporite minerals of Sirjan playa, Iran were mapped using Advanced Spaceborne Thermal Emission and Reflection Radiometer (ASTER) and Landsat 8 images. Spectral angle mapper (SAM) was applied to map evaporite minerals of the study area. Two kinds of reference spectra were used for classifying the images that consist of: (1) recorded reflectance spectra of evaporite minerals and (2) image-derived spectra which were acquired from images based on GPS coordinates of samples. Determination of evaporite minerals assessed by X-ray diffraction (XRD) on field samples which were collected in October 2015 when the lake was completely dry. After image classification, the overall accuracy of 95.27% for Landsat 8 images and 91.81% for ASTER images were achieved, respectively, using image-derived spectra. SAM classification using samples' spectra showed lower accuracy of 85.96 and 80.31% for ASTER and Landsat images, respectively. Therefore, the image-derived spectra produced better classification accuracy. For determining the main source of inflows of the sediments into the playa, drainage system of Sirjan basin, that was derived using digital elevation model, false color composite image, mosaic of old aerial photographs and map of evaporite minerals were used. It showed that the main source of inflows of the sediments to the playa is from volcanic and sedimentary rocks of Urumieh-Dokhtar mountains located in the north-east and eastern parts of the playa.

Keywords Evaporite minerals · Sirjan playa · Spectral angle mapper · Source rocks

✉ Hojjatollah Ranjbar
h.ranjbar@uk.ac.ir

Azam Soltaninejad
soltani_nejad@yahoo.com

Mehdi Honarmand
mehonarmand167@yahoo.com

Sara Dargahi
dargahis@yahoo.com

[1] Department of Geology, Shahid Bahonar University of Kerman, Kerman, Iran

[2] Department of Mining Engineering, Shahid Bahonar University of Kerman, Kerman, Iran

[3] Department of Ecology, Institute of Science and High Technology and Environmental Sciences, Graduate University of Advanced Technology, Mahan, Iran

[4] Department of Geology, Shahid Bahonar University of Kerman, Kerman, Iran

Introduction

Arid and semiarid lands account for more than one third of the land surface of the Earth. The greatest belt of arid and semiarid regions extends across North Africa in the Sahara, through the Arabian Peninsula with the "Rub Al Khali" of extreme aridity, into the salt deserts of Iran and the Takla Makan of Central Asia. Playa environments are depressions in land areas in which evaporite minerals form. By definition, for an evaporate salt to precipitate, liquid water loss from a brine mass must exceed inflow and the brine concentration process should be caused by solar evaporation (Warren 2006, 2010).

All the Iranian playas are located in areas where the annual evaporation is significantly greater than annual precipitation. When evaporation of water in playa increases, salt concentration increases until crystals of salts begin to precipitate at its saturation point. In a closed hydrological system the composition of concentrated lake brines

largely depends on unstable lithologies that are leached and altered by inflow waters in the drainage basin surrounding a salt lake (Eugster 1980; Hardie and Eugster 1970).

Most exploited evaporate salts and their associated brines are used in various chemical industries. Volumetrically, halite (rock-salt) is the most utilized evaporite mineral. Many playas contain large deposits of saline minerals formed by precipitation from standing brine or by replaced growth within brine-saturated clastic sediments (Eugster and Hardie 1978). Such deposits are major sources of industrial minerals, including halite, gypsum, sodium and magnesium sulfates, borax, lithium concentrates, etc. (Reeves 1978). Based on the wide usages of evaporites, the importance of the study of these types of resources is obvious. One of the most important ways of the studying of evaporites, as an efficient way especially in the arid environments where consist of less or no vegetation, is application of remote sensing.

Remote-sensing techniques are important tools for playa studies. Multispectral images have strong potential for use in mapping efflorescent salts that exhibit short-wave infrared (1–2.5 μm) and thermal infrared (8–12 μm) spectral absorption features related to hydrogen-bonded water molecules and to hydroxyl, carbonate, sulfate, and borate anion groups (Crowley 1991; Ross 1974; Salisbury 1991). Short-wave infrared spectra are also very sensitive to minor hydrate minerals of natural component of natural salt mixtures and to moisture variations across playa surface (Crowley 1993). Remote sensing studies also can be used for determining evaporation potential of the Earth's surface. Miralles et al. (2011) based on satellite data used Priestley and Taylor (PT) evaporation model for estimating evaporation potential of earth surface.

There are many studies of VNIR spectral measurements in which saline minerals have been considered (Clark et al. 1993; Crowley 1991; Drake 1995; Hunt 1977; Mougenot et al. 1993; Vane and Goetz 1988). Hunt and Salisbury (1971) in their studies, recorded VNIR reflectance spectra of some of these minerals such as gypsum, bassanite, halite, thenardite, and several borate minerals. Hunt and Salisbury (1971) and Gaffey (1987) studied the VNIR spectra of anhydrous carbonate minerals, such as calcite, dolomite, and magnesite. Crowley (1991) recorded visible and near-infrared (VNIR: 0.4–2.4 μm) reflectance spectra for 35 saline minerals which were in a wide range of mineral and brine chemical compositions that can be found in playa evaporite settings and the result of this study showed that many of saline minerals exhibit diagnostic near-infrared absorption bands, chiefly attributable to vibrations of hydrogen-bonded in structural water molecules. According to these results, he stated that the use of spectral reflectance measurements in playa studies should aid in mapping evaporite mineral distributions and may provide insight into the geochemical and hydrological controls on playa mineral and brine development. Crowley (1993) studied efflorescent salt crusts in Death Valley, California, and mapped saline minerals by using airborne AVIRIS data and the results of this study demonstrated the potential for using AVIRIS and other imaging spectrometer data to study playa mineralogy. Howari et al. (2002) measured spectral reflectance upon salt crusts on two kinds of soils with a spectroradiometer in the visible and near-infrared region (400–2500 nm) and reported the absorption position of some evaporite minerals. The results of this research showed that crystal size or salt concentrations did not affect the positions of the absorption bands of the salt crusts, whereas reflectance increased as particle sizes decreased or with increasing presence of salt crust. Kavak (2005) studied the usefulness of ASTER and Landsat ETM+ imageries for mapping deposits of massive Oligocene gypsum in Sivas Basin, Turkey using various processing methods and the results showed that the ASTER and Landsat ETM+ multispectral systems have superior capabilities for differentiating evaporitic sediments in this area. Öztan (2008) and Öztan and Süzen (2011) applied common remote sensing mapping techniques such as band ratio (BR), decorrelation stretch (DS), feature-oriented principal component analysis (FOPCA) and thermal indices on ASTER images to map gypsum and reported that all methods were successful in mapping evaporates, but TIR data from ASTER when used as a Sulfate Index (SI) yielded a more refined result than other methods. Caceres et al. (2008), using ASTER imageries and applying classification methods, showed that a detailed mineral mapping in evaporitic environments such as Sud Lipez Salt Lakes in Bolivia can be achieved with high confidence and good spatial accuracy. Özyavaş (2016) applied ASTER SWIR bands and adopted image processing techniques such as decorrelation stretch, band ratio, and feature-oriented principal components selection (FPCS) for mapping both gypsum and carbonate rocks along the Salt Lake Fault, Turkey. Comparison of their resulted images with the geologic map of the study area demonstrated that the gypsum and carbonate rocks were clearly identifiable using ASTER images.

Geochemical analyses are useful methods for studying the origins of evaporites. The behavior of main ions in the evaporation process is described by Hardie and Eugster (Eugster and Hardie 1978; Hardie and Eugster 1970). The model that they suggested interprets the chemistry of water undergoing evaporation in terms of a succession of geochemical divides. Successive water types depend on initial water chemistry and molar ratios of principal ions (Drever 1997). The brine chemical analysis of Gavkhoni Playa, Iran (Pakzad and Ajalloeian 2004) showed that the brine has

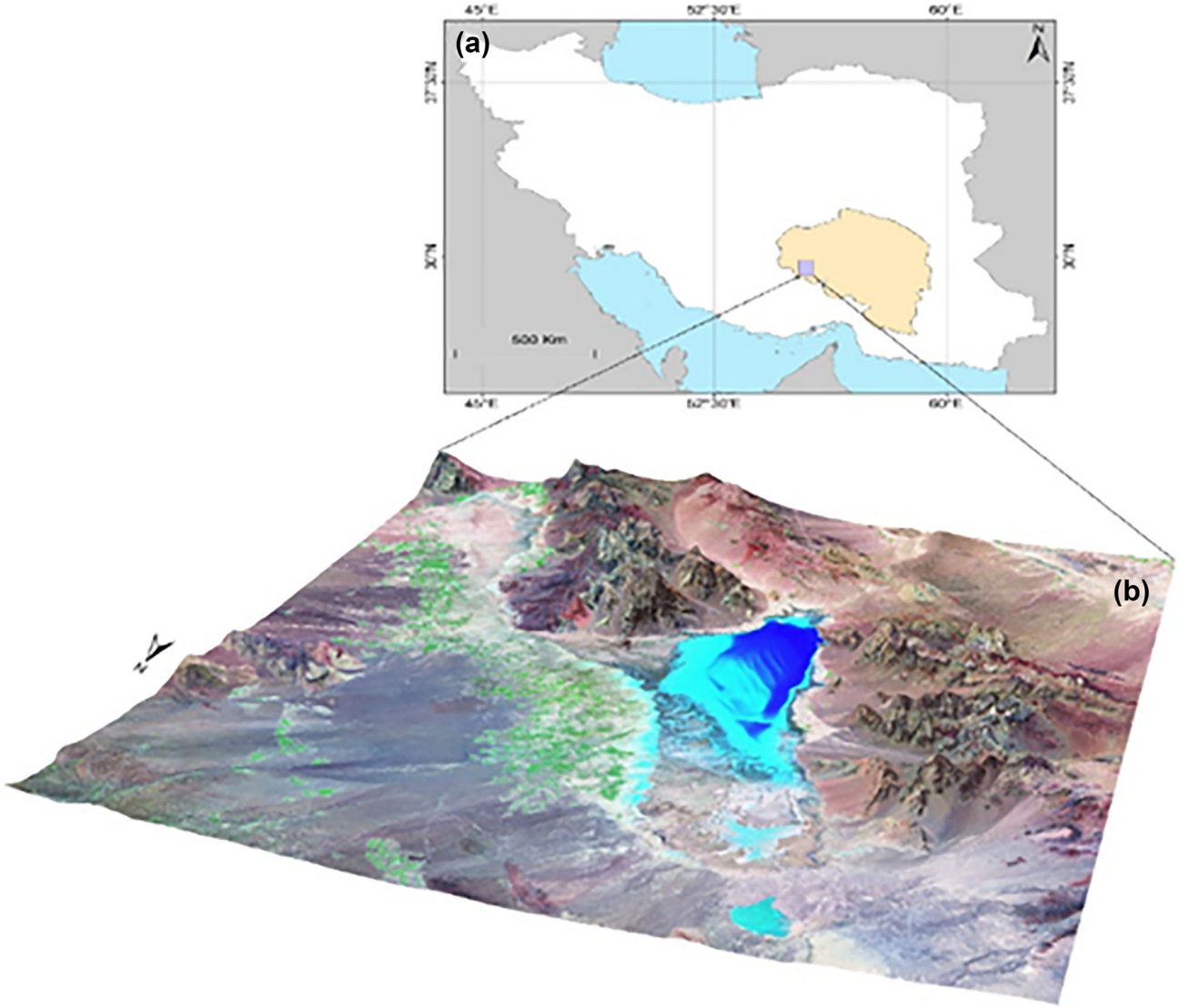

Fig. 1 **a** Location of the study area, **b** general view of the study area

become progressively depleted in carbonate and sulfates from the margins to the center of the lake. It ultimately became a Na^{+}, (Mg^{2+}), Cl^{-} brine type in the northern section and a Na^{+}, Mg^{2+}, Cl^{-} brine type in the central part of the lake. After complete desiccation, the mineral assemblage exhibited halite, carnallite, bischofite, and tachyhydrite in abundance. Roy and Smykatz-Kloss (2007) studied the rare earth elements (REE) systematics in nine different playa sediments of the Thar Desert and the result of this study showed the dissimilarity in the degree of HREE fractionations both in the eastern and western playa sediments and it was attributed to the differential distribution of minerals, depending upon their resistance to chemical weathering. Precipitated efflorescent salts in Cu–Co chemical leaching plant wastes in Kabwe, Zambia, have been studied using X-ray fluorescence (XRF) analysis, scanning electron microscopy (SEM), Raman spectroscopy, and evaporation experiments combined with geochemical modeling. The result of this study revealed a strong enrichment of Cu and Co salts. Using XRD analysis they compared the field-collected minerals with minerals that were precipitated from the brine in experiment and based on these studies the model of evaporation was reported for the study area (Sracek et al. 2010). Keskin et al. (2016) based on the geochemical and isotopic studies of sediment samples which were collected from the gypsum and stromatolite of the Tertiary series of evaporites in the Ulukış¸la Basin, Central Anatolia, Turkey showed that in this area, marine waters mixed with fresh continental waters periodically and these conditions caused the formation of stromatolites and a thick sequence that in time became evaporites.

Desert crusts and salt crusts are two features that have been recognized in the Iranian deserts. Desert crusts or soil

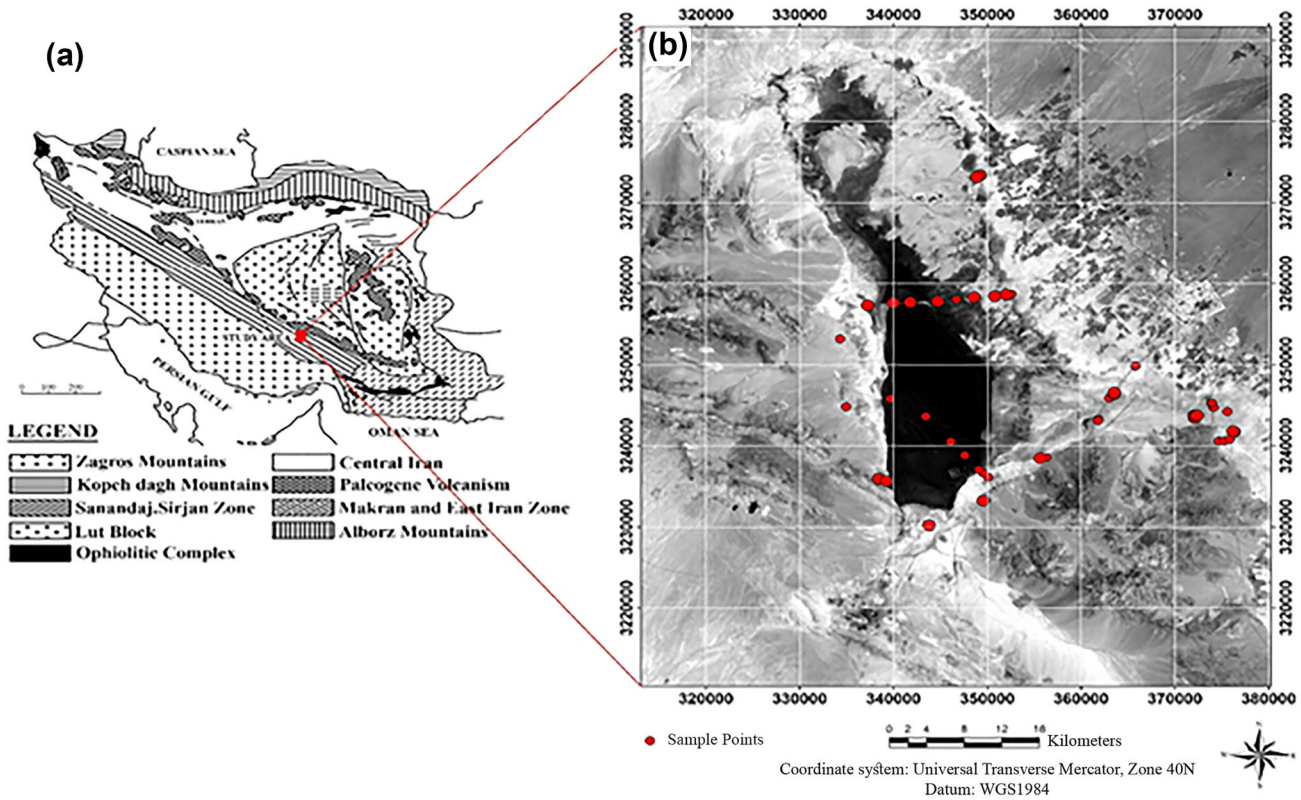

Fig. 2 **a** Structural zones of Iran (Stocklin 1968) and **b** Sampling points shown on ASTER band 6

crusts which are usually up to 3–5 mm thick, have a bright surface and salt crusts are the result of evaporation from shallow water table. Iran contains many arid areas such as Damghan, Kashan, Maharloo, Qom, Ardakan, Qazvin and Sirjan which are studied mainly for their morphological and environmental aspects, but the salt crusts as a source of non-metallic materials have not received much attention. The main reason may be related to the limitations of transportation and harsh climate. Most of the researches on the desert areas of Iran were focused on detecting and mapping soil salinity (Alavipanah et al. 2004a, 2004b, 2010, 2011; Alavipanah 2000; Alavipanah and Pouyafar 2005; Matinfar et al. 2011; Zehtabian et al. 2002).

There are few remotely sensed studies on Sirjan playa. Krinsley (1970) studied Iranian playas including Sirjan playa based on aerial photographs and separated different geomorphic surfaces, based on morphological properties and size of sediments. Farpoor et al. (2012) focused on Sirjan soil–geomorphology relationships and the effect of past and present climate on soil formation in this area.

The main aim of this study is to map evaporite minerals using spectral angle mapper (SAM) method on ASTER and Landsat 8 multispectral data based on two types of spectra for Sirjan playa. The inputs spectra consist of: (a) spectra which were recorded on an ASD Field Spec3® Spectroradiometer, and (b) spectra which were acquired from the satellite images. Finding the source rocks for these evaporite minerals based on remote sensing and geomorphic data is another aim of this study.

Study area

The study area is located in Iran, south-west of Kerman Province and spreads between 29°20′ to 29°30′ north latitudes and 55°30′ to 55°40′ east longitudes. This Playa which is the largest playa (1625 km^2) in the Kerman Province, occupies a triangular-shaped depression and contains a clay flat (68%) and a salt crust (32%) (Fig. 1). This playa is surrounded by Urumieh-Dokhtar and Sanandaj-Sirjan structural belts.

In the northern part of the playa a small island has been exposed which is composed of Eocene volcanic rocks and Krinsley (1970) has noticed several ancient beachlines on it and the highest beachline estimated 5 m above the existing salt crusts. He reported that Sirjan playa is the remnant of an ancient large lake. The playa is surrounded by alluvial plains in the north and eastern parts. These alluvial plains have been created by joining alluvial fans. These plains continue from mountains slope to the playa and sediments grain sizes decrease from the mountains slope towards the playa. West and south-west alluvial plains are less

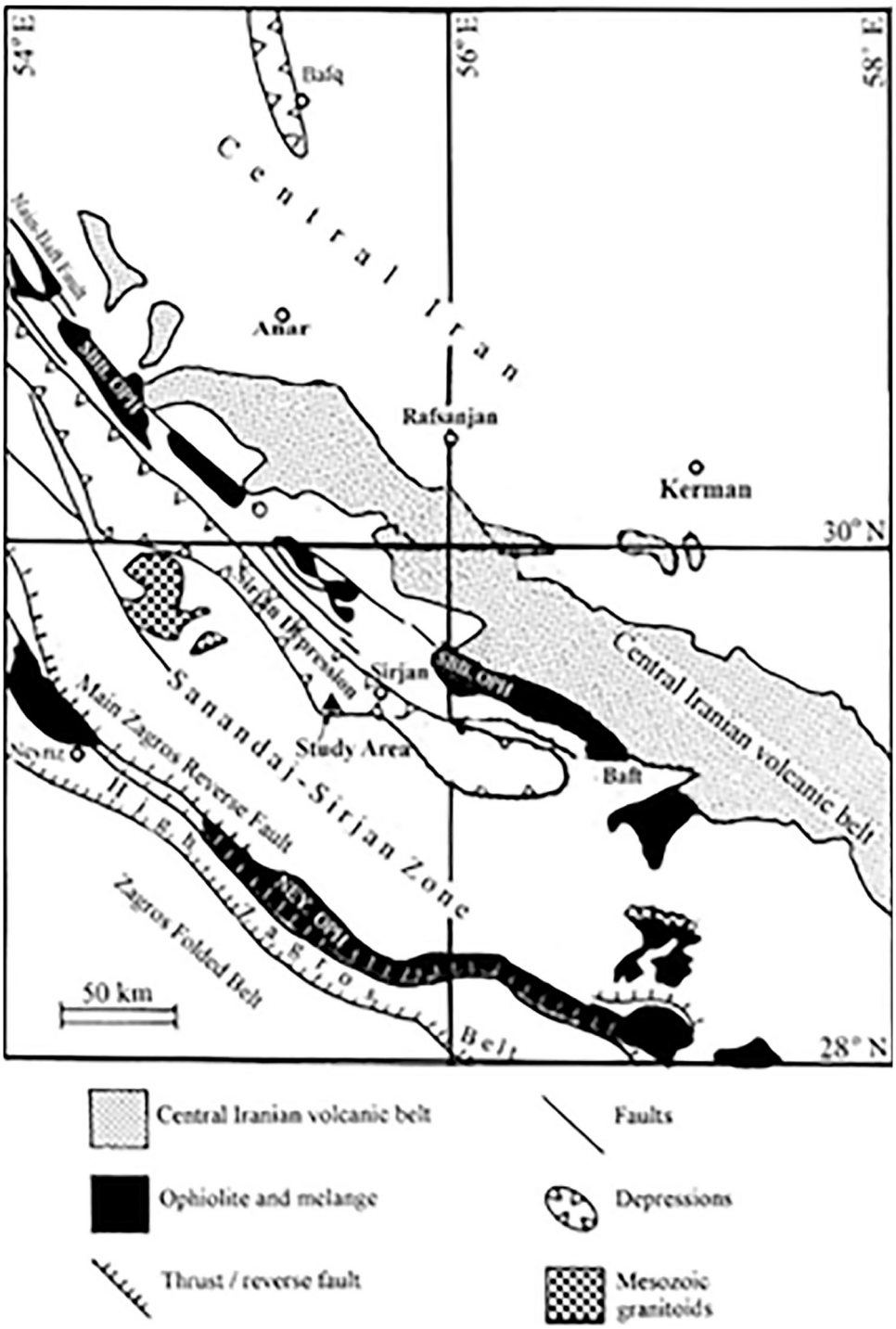

Fig. 3 Simplified structural map of the area that shows the location of Sirjan depression (modified after Shahabpour 2005). Coordinate system: Geographic Coordinate System, World, Datum: WGS 1984

expanded. Fans are considerably more active along the north-east margin of the playa, adjacent to the highest slopes in this part of the basin.

The southwest and southeast fans are only locally active. The drainage system is often active during seasonal floods and they are generally dry for the rest of the year. A remarkable aspect of the salt crust is its sharp contact with both fans and clay flat. The salt crust is in immediate contact with the fans or debris slopes where the adjacent land is steep. The salt crust is estimated to contain polygons over 50% of its area. Some of these, particularly in the southern area, are up to 60 m in diameter and in turn include smaller polygons (Krinsley 1970).

Sirjan playa shows a mineral zonation as other playas. Chloride minerals are concentrated in the center of the

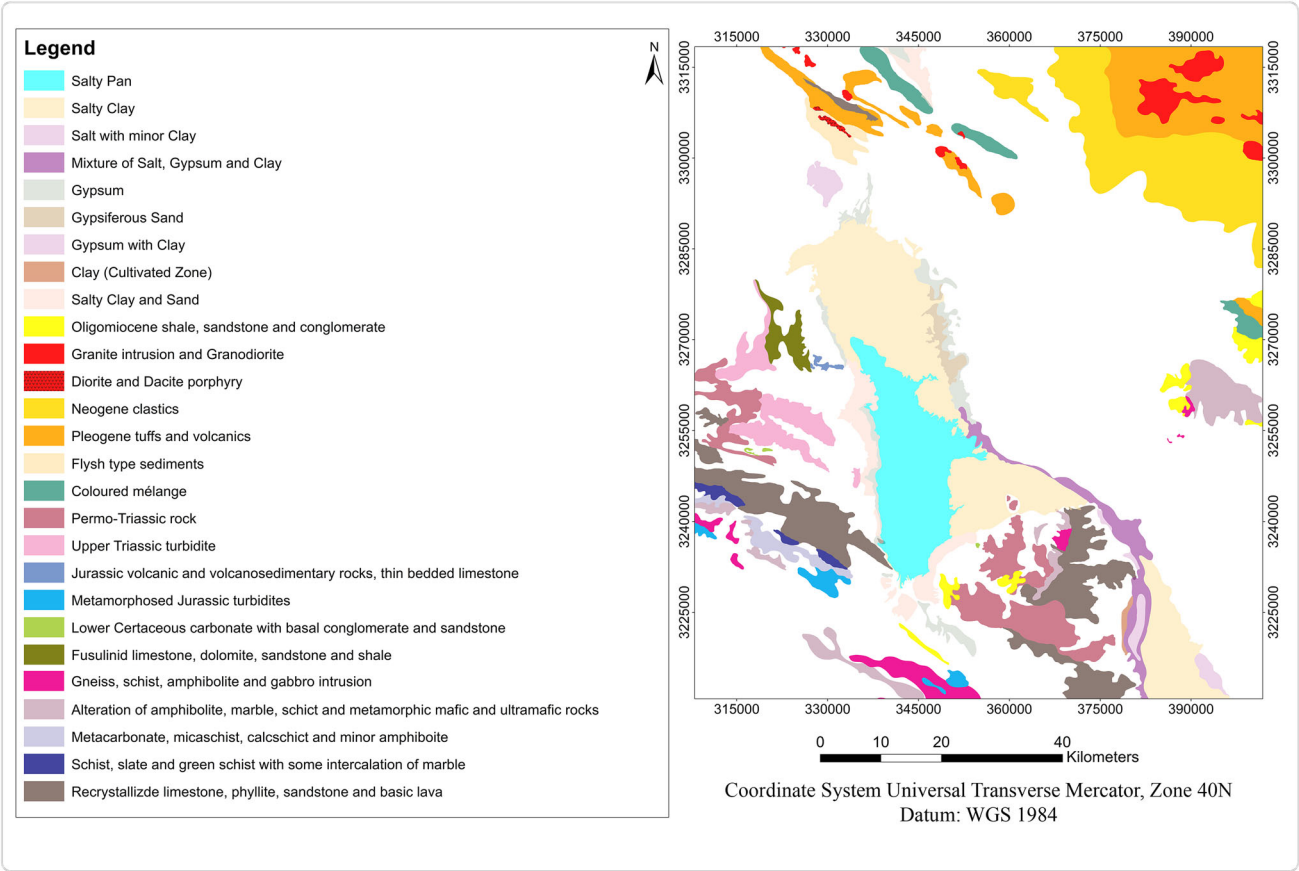

Fig. 4 The simplified geological map of Sirjan area.Compiled from the maps by Dimitrijevic et al. (1971), Roshan Ravan et al. (1996), Sabzehei et al. (1997) and Sheikholeslami (2015)

playa and towards the rims, sulfates and carbonates present, respectively. Concentration of sulfate minerals is like a strip which surrounds the playa (Nazemzadeh Shoaei and Azizan 1990).

The playa is located in a depression between Sanandaj-Sirjan and Urumieh-Dokhtar structural zones (Fig. 2). This depression is called Sirjan depression (Fig. 3) and formation of this depression is related to the evolution of the orogenic belt of the area. During Upper Permian—Late Triassic closure of Paleotethys, by the northward motion of the micro-continents (Central Iran, central Afghanistan, Nuristan, Pamir) resulted their welding with the Eurasian plate. At the same time with the closure of Paleotethys in the north, rifting occurred along the present Zagros thrust zone of the continental plate and it caused the opening of a new ocean which is called Neotethys. Disappearing of Paleotethys caused the floor of Neotethys started to subduct beneath the Eurasian plate during Triassic—Jurassic time. This led to a metamorphic event in Early Cimmerian which was recorded in the southwest Sanandaj-Sirjan zone and also emplacement of intrusive bodies within this zone in Upper Triassic. The final closure of Neotethys and therefore the collision of Arabia plate and central Iran took place during the Neogene. The Sirjan depression which is located between the Sanandaj-Sirjan zone and the Central Iranian volcanic belt is considered an inter-arc basin in which sirjan playa is located (Shahabpour 2005). Inflow water from north-east of the playa passes through a part of Urumieh-Dokhtar rocks and their derived sediments. The altitudes in the Urumieh-Dokhtar part is over 3000 m and altitudes in the plains are between 1700 and 2000 m. The oldest units of this part are Eocene rocks that belong to the upper part of the volcanogenic complex, represented by pyroclastics and lava flows, which correspond to pyroxene trachy-andesites, less frequently pyroxene-andesites and trachy-basalts. The plutonic rocks form discordant hypabyssal massifs and stocks in the Eocene complex, accompanied by numerous intrusive bodies. The intrusives vary from monzonitic, with rare transitions into grano-syenites and syenites to granodioritic with transitions into quartz-diorite, diorite and less frequently, into monzonite and quartz-monzonite. Oligocene–Miocene sediments crop out in the south-eastern and eastern parts of the playa, overlying unconformably the Eocene formation which are sandy limestones and intruded by several generations of Paleozoic to Cenozoic intrusions (Sheikholeslami 2015).

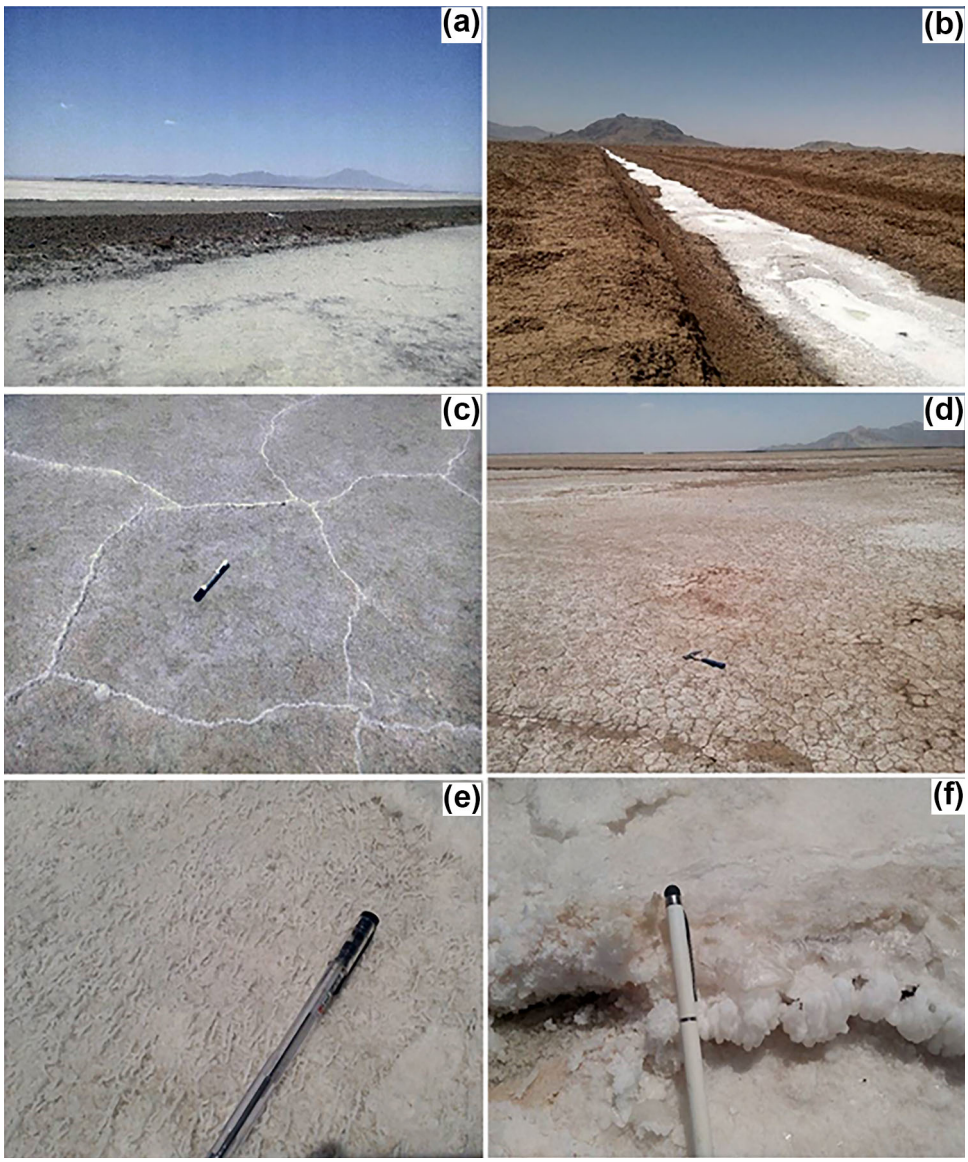

Fig. 5 Salt crust of Sirjan playa: **a** the photo has been taken beside the road across the middle of the playa, **b** salt stream in western part of the playa, **c** salt polygons in the playa, **d** salt encrusted puffy ground in Sirjan playa, **e**, **f** textures of salt in the salt crust

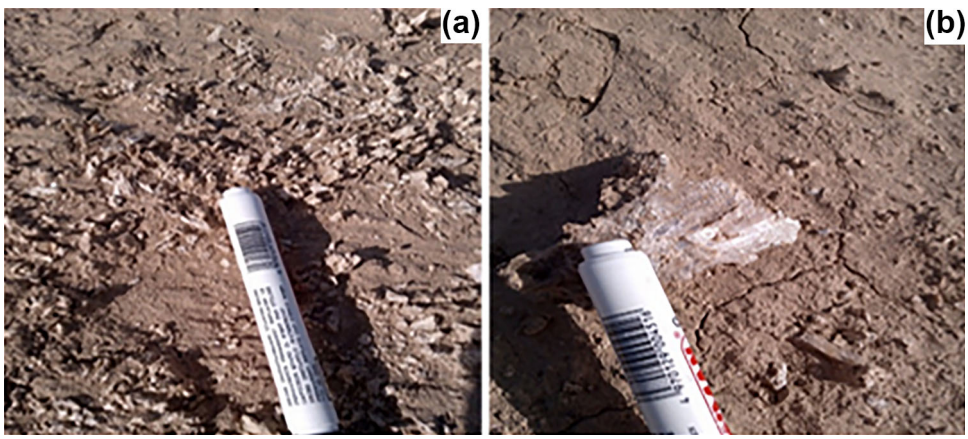

Fig. 6 Gypsum crystals growth on the ground

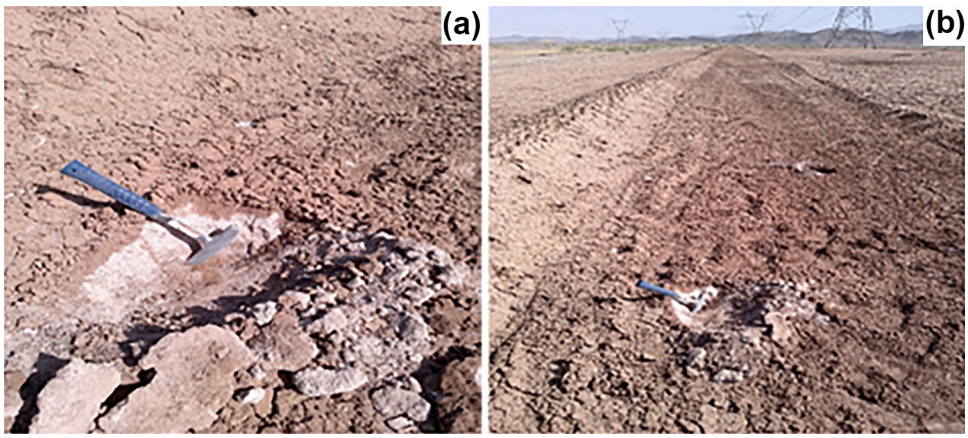

Fig. 7 Thenardite occurrence in the southeastern part of the study area

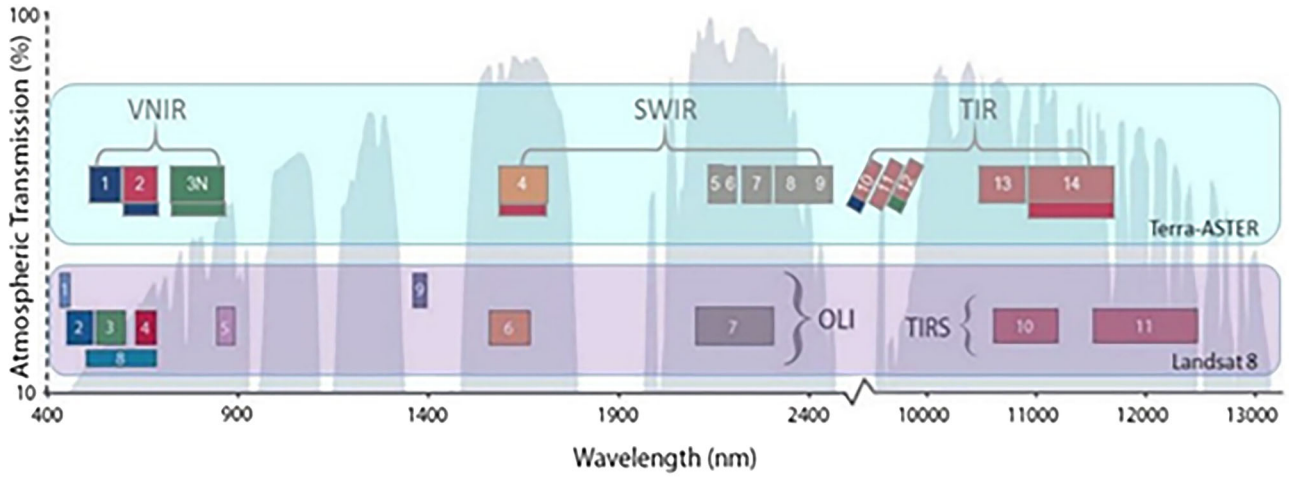

Fig. 8 ASTER and Landsat 8 spectral bands' comparison (Duda and Daucsavage 2015)

Table 1 Acquisition dates of satellite images and aerial photographs used for this study

	Satellite image	Date
1	ASTER	25 July 2001
2	Landsat 8	28 May 2015
3	Aerial photographs	October 1956

The oldest rock units are Paleozoic metamorphic rocks, which are deformed and metamorphosed under greenschist to amphibolite facies, Sandstones and siltstones. Neogene sedimentary members, separated by an unconformity, have been identified in the Neogene succession. The lower member is composed mainly of medium- to fine-grained sandstones with gypsum veinlets and halite intercalations. The upper member consists of loosely consolidated or almost unconsolidated, unsorted and poorly stratified sediments (Dimitrijevic et al. 1971).

In the south, southwest and west of the playa deformed and metamorphosed rocks of Sanandaj-Sirjan zone are present (Berberian and King 1981; Stocklin 1968). It mainly consists of Paleozoic–Mesozoic metamorphic rocks, Devonian marbles and minor greenschist. Alternation of black schist, quartzite, mica schist and thin bands of marble belong to Carboniferous to Late Devonian units in the area. Metamorphosed to non-metamorphosed turbiditic deposits of Triassic and Jurassic and Jurassic volcanic rocks overlay Devonian units. Lower Cretaceous carbonates, Cenozoic turbidites, carbonate and detrital succession of Oligocene–Miocene age, Bakhtiyari Formation of Late Pliocene age and finally Quaternary deposits, cover previous rocks (Nazemzadeh Shoaei et al. 1996; Sheikholeslami 2015) (Fig. 4).

Data and methodology

Field work and sampling

Field work is one of the most important steps in a research, especially in the case of evaporate areas, because the time

of sampling is very important. We tried to collect the samples in the driest time (May–June 2015). Location of samples which were collected are shown in Fig. 2. Figures 5, 6, and 7 shows some the of field photos of the study area that depicts surface exposures of different evaporite minerals. To determine the mineralogical composition, samples were analyzed by XRD. The spectra of samples were recorded by Field Spec3® which is a field portable, precision radiometer with a spectral range of 350–2500 nm.

Satellite and aerial data

Landsat 8 and ASTER images were used here for this study. The specifications for these images are presented in Fig. 8 and acquisition date of these images are given in Table 1. Acquisition date of Landsat 8 is on the exact day of sampling.

For detecting the source of influx to the playa about 300 sheets of aerial photographs which were taken in 1956 were mosaicked. Digital elevation model (DEM) derived from ASTER data was used here for generating 3D model of the area.

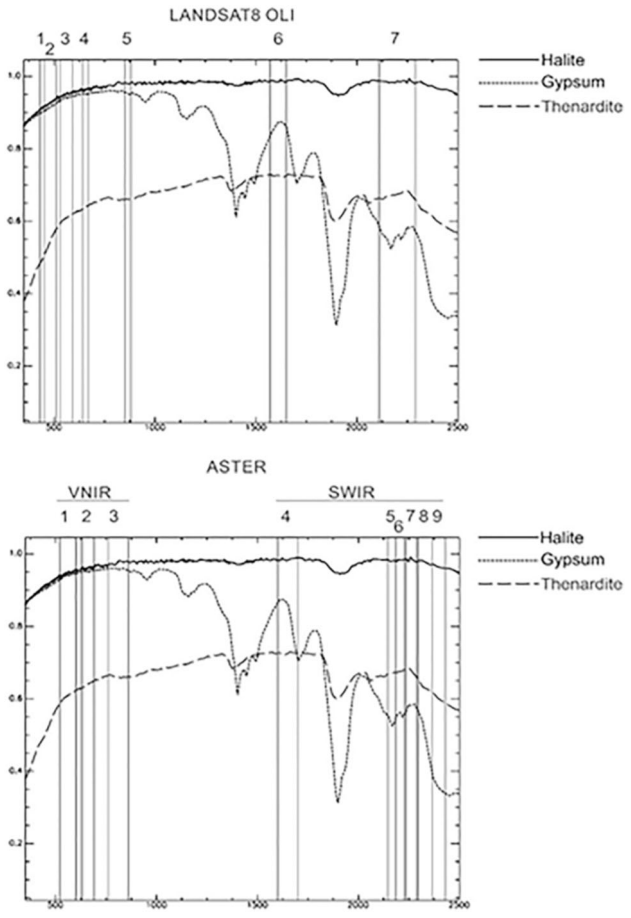

Fig. 9 Spectral response curves of Halite, Gypsum and Thenardite with location of Landsat 8 and ASTER spectral bands (source of data: Clark et al. 1993)

Image pre-processing

The images were checked for cloud cover and sensor errors such as banding and other geometric distortions. The images were supplied in terms of scaled radiance at-sensor data, and for this study atmospheric corrections were applied.

In this study, for ASTER data, Fast Line-of-sight Atmospheric Analysis of Spectral Hypercubes (FLAASH) correction was used on the visible, near-infrared and short-wave infrared bands. FLAASH atmospheric correction method, makes it possible to accurately compensate atmospheric effects. FLAASH provides a collection of spectral analysis and atmospheric retrieval methods and corrects wavelengths in the visible through near-infrared and short-wave infrared regions, up to 3 μm (Perkins et al. 2005). Cross-talk correction was also applied on ASTER data before applying FLAASH correction. After atmospheric correction, selected bands were stacked and resampled at 30 m by the bilinear method. For Landsat ETM+ data, internal average relative reflectance (IARR) was applied to bands one to seven for Landsat 8. This method calculates the average radiance for each band of the image therefore it creates an average spectrum and divides it into actual radiance for each band of each pixel, to create an image of apparent reflectance. It has been suggested to be the best method for arid areas with no vegetation cover (Kruse 1988). After atmospheric correction, ASTER images were georeferenced in the universal transverse Mercator (UTM) projection using WGS-84 ellipsoid as datum.

Spectral properties of evaporites minerals

Absorption features that have unique position, size or shape, provide the most important information for recognizing minerals through image processing techniques. If a spectrum contains more than one absorption feature the spacing between these features can also provide diagnostic information. A spectrum is considered diagnostic if it differs from the spectra of other evaporite minerals (Drake 1995). Reflectance spectra can be recorded rapidly in the field, permitting in situ measurements of fragile mineral species that may not be sufficiently stable for transport to a laboratory. Reflectance measurements also require little sample preparation. Grinding can cause dehydration and other structural changes in the saline minerals typical of playa setting. Crowley (1991) recorded reflectance spectra of 35 saline minerals that represent the wide range of mineral and brine chemical compositions found in playa

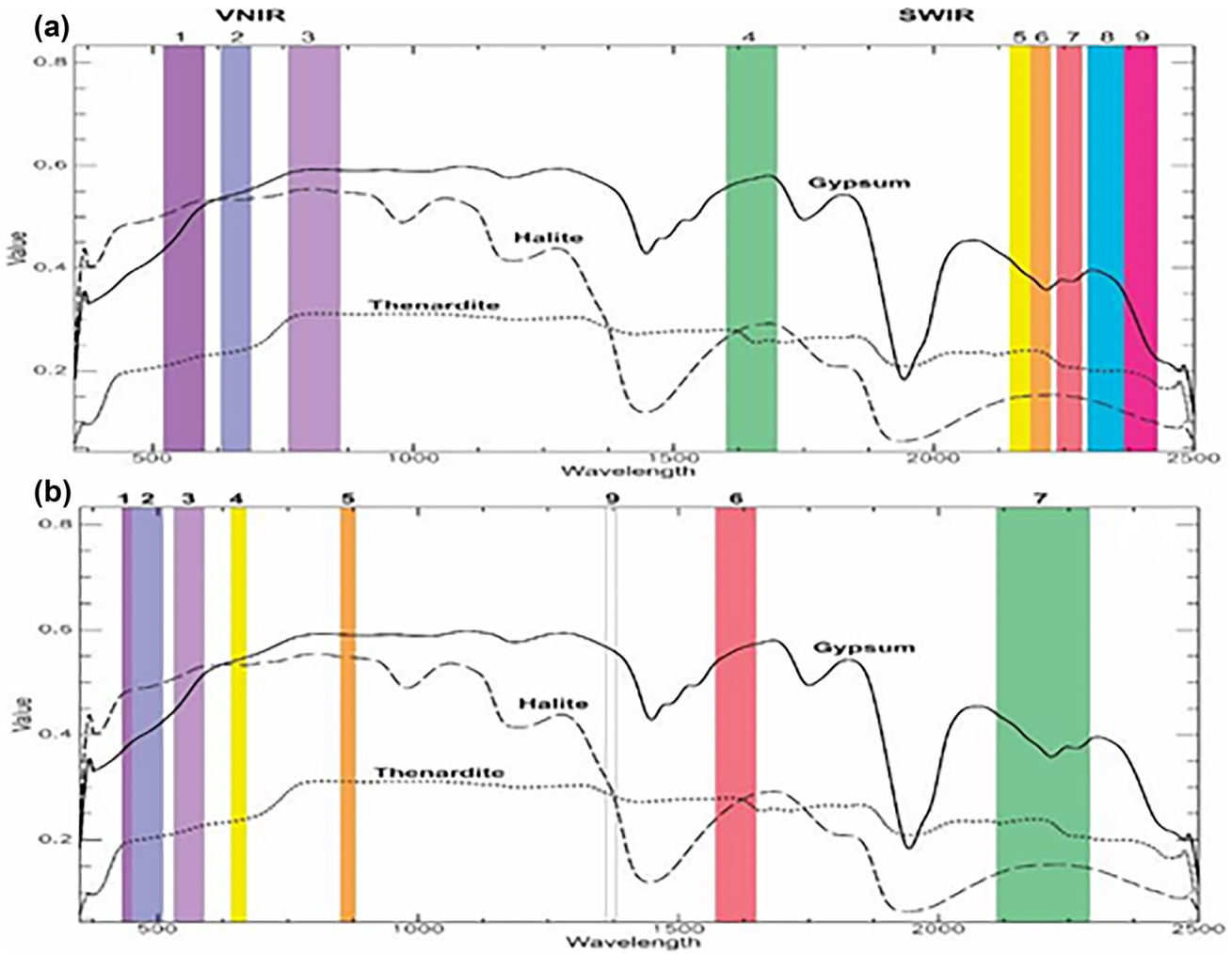

Fig. 10 Reflectance spectra of halite, gypsum and thenardite minerals. The positions of spectral bands for each sensor are shown with color strips: **a** ASTER bands, **b** Landsat 8 band

evaporite settings and reported that many evaporite minerals exhibit diagnostic VNIR absorption features, mainly related to hydrogen-bonded water molecules, and to carbonate and borate anion groups contained in the mineral structures. Strongly hydrated minerals shows relatively broad absorption features caused by the overlapping bands of water molecules in numerous different bonding configurations. Species containing less water, such as gypsum ($CaSO_4{\cdot}2H_2O$) show narrower absorption features indicative of fewer discrete sites for water molecules and less absorption band overlap. Drake (1995) evaluated the spectral response of evaporite minerals to determine minerals that can be identified and mapped by remote sensing and emphasized that spectral diversity exhibited by evaporite minerals suggests numerous applications in spectroscopy and remote sensing.

The spectrum of gypsum shows major absorption features in the visible and near-infrared (VNIR) and SWIR regions due to overtones and combination tones of molecular water (Hunt and Salisbury 1971). The absorption features between 1.4 and 1.6 μm are due to the first overtone of the O–H stretching fundamental and the strong absorption features near 1.9 μm are due to a combination of the O–H stretching and the H–O–H bending fundamentals. (Öztan 2008).

Csillag et al. (1993) studied the reflectance spectra of salt affected soil samples of California and Hungary. Their study showed the ranges of detecting the salts. The portions of the spectrum in which common evaporite minerals have diagnostic features include the visible (550–770 nm), near infrared (900–1030 nm, and 1270–1570 nm) and the middle infrared (19,402,150 nm, 2150–230 nm, and 2330–2400 nm). From 500 to 1850 nm, the spectra of halite are almost featureless and in this region, the spectra have a plateau shape with high reflection values. Two weak observed absorption features in this region are at 994 and 1151 nm. Two major absorption features of halite appear at 1457 and 1958 nm. According to Mougenot et al. (1993)

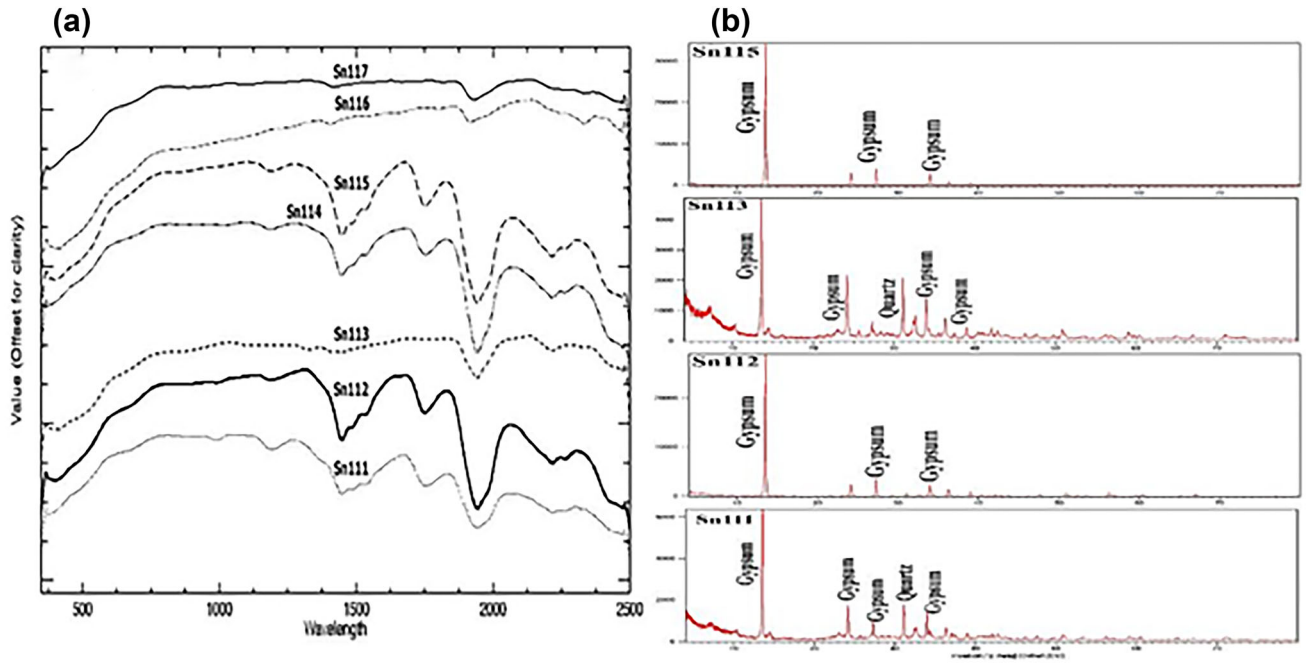

Fig. 11 **a** Laboratory reflectance spectra of some gypsum samples of the study area, **b** XRD of the same sample

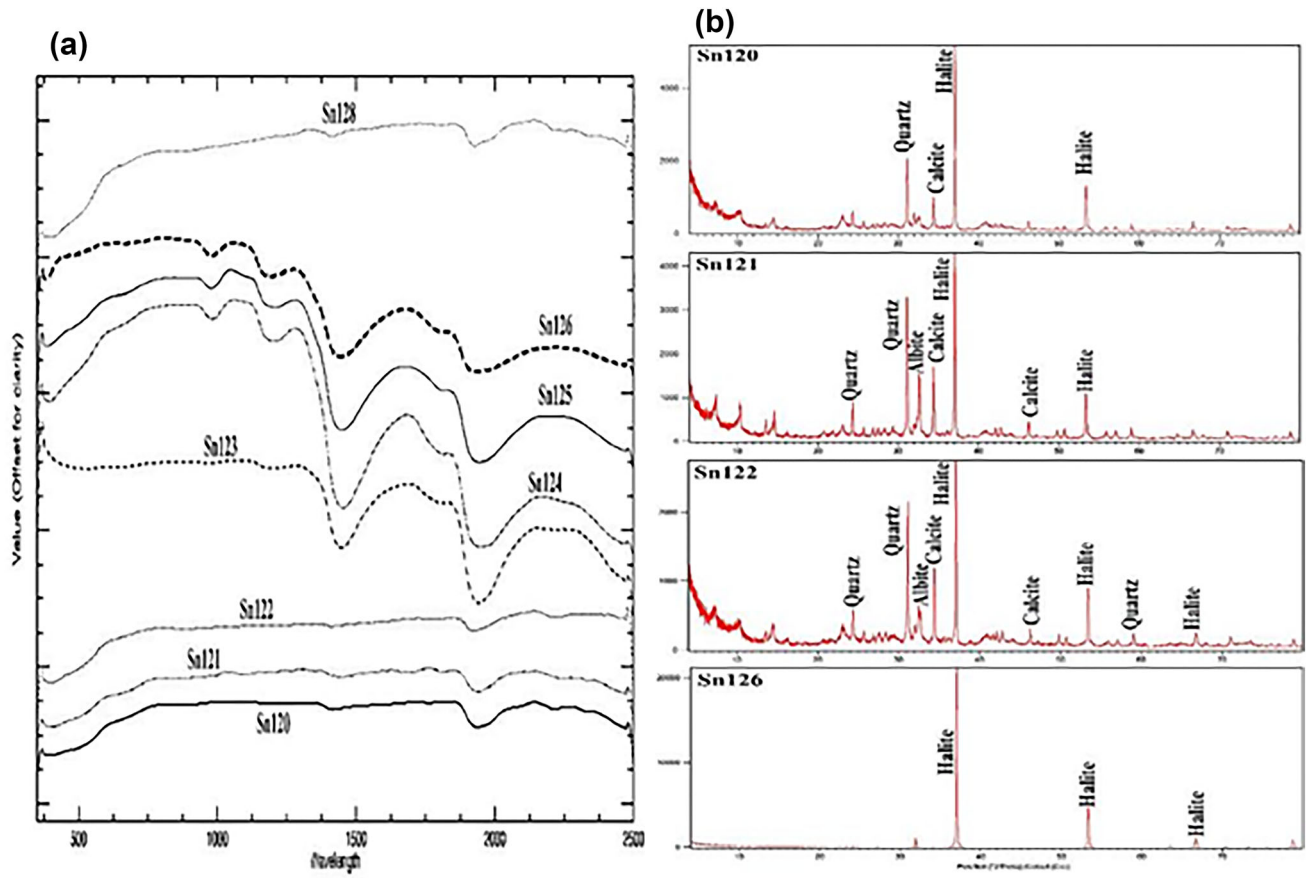

Fig. 12 **a** Laboratory reflectance spectra of some halite samples of the study area, **b** XRD of the same sample

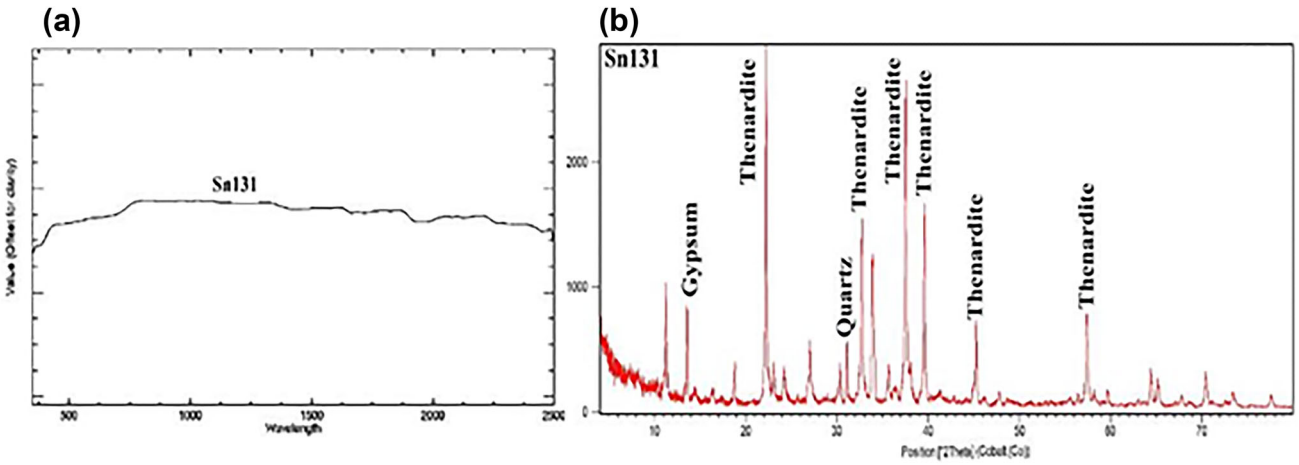

Fig. 13 **a** Laboratory reflectance spectra of thenardite sample of the study area, **b** XRD of the same sample

because of being a transparent salt, its chemical composition and its cubic crystal system, halite cannot present strong absorptions in the visible and near to thermal infrared bands. Hunt and Salisbury (1970) concluded that halide ions possess no internal vibration modes, and the absorption features all occur in the far infrared and the absorption features of this mineral are attributed to the water in its fluid inclusions. Spectral response curves of Halite, Gypsum and Thenardite with location of Landsat 8 and ASTER imagery bands based on Clark et al. studies are shown in Fig. 9.

In Sirjan playa based on XRD analysis, three types of evaporite minerals were distinguished. The most abundant evaporite mineral is halite. Gypsum and thenardite are also relatively abundant in this area. Reflectance spectra of samples from the study area were recorded by Field Spec3® spectroradiometer. Typical reflectance spectra of these samples are shown in Fig. 10. The position of ASTER and Landsat 8 selected spectral bands are plotted on these curves.

VNIR and SWIR absorption features are caused by two main processes of electronic transitions and molecular vibrations (Hunt 1977). Most of the absorption features of saline minerals are vibrational and are due to vibration of molecular groups such as carbonate, sulfate, hydroxyl anion groups, borate, and water molecules. Among these groups, water molecules are more important, but for anhydrous minerals like halite and thenardite, absorption features are related to the presence of fluid inclusions and/or adsorbed water (Crowley 1991; Howari et al. 2002).

Crowley (1991) revealed that halite samples have main absorptions on 1432 and 1936 nm, gypsum absorption positions are located on 992, 1196, 1440, 1484, 1530, 1740, 1768, 1936, 1964 nm and thenardite absorptions are on 1410 and 1922 nm. Howari et al. (2002) found that samples of gypsum crusts have diagnostic absorption features near 1023, 1225, 1457, 1757, 1800, and 2336 nm, whereas halite crusts have diagnostic absorption features near 1442, 1851, 1958, thenardite absorption are on 1234, 1486, 2103 nm. In this study, the absorption position of halite, gypsum and thenardite were recorded. Some of gypsum, halite and thenardite measured spectra and their XRD results of the study area are presented in Figs. 11, 12 and 13.

In the study area, halite and gypsum are abundant and they are well exposed on the surface, but thenardite is less abundant and its form of occurrence makes its detection by remote sensing difficult, because it forms as a layer about 10 cm under the surface (see Fig. 7) and in some places, it has surface exposure. Table 2 lists the wavelength positions of major absorption bands for these minerals.

Image processing

Digital image classification techniques are used to classify each individual pixel of an image based on the spectral information to create lithological or geological maps (Kruse et al. 1993). Image classification methods can be divided into statistical classification algorithms that use summary class statistics based on groups of image pixels, and spectral analysis techniques that match image spectra to previously acquired field or laboratory spectra, known as spectral libraries (Landgrebe 2000).

The SAM is a tool that permits rapid mapping of the spectral similarity of image spectra to reference spectra. The reference spectra can be either laboratory or field spectra or extracted from the image. The spectral similarity between two spectra is measured by calculating the "angle" between the two spectra, treating them as vectors in a space with dimensionality equal to the number of bands. A simplified explanation of this can be given by considering a

Table 2 Absorption wavelength of gypsum, halite and thenardite samples for Sirjan playa

	Sample	Wavelength of absorption (nm)																				
Gypsum	Sn111	991		1187			1449	1487	1537		1750		1945	1983	2118	2264						
	Sn112	989		1187			1449	1487	1535	1654	1749		1943		2216	2266						2427
	Sn113	854	1106			1324	1449	1479					1941		2216		2324					2429
	Sn114		1023	1185			1448	1486	1537		1750		1943	2218	2267							2436
	Sn115	868	995	1190			1448	1487	1535		1750		1945	2218		2269						2429
	Sn116				1260	1343	1405			1663		1806	1920		2256	2335	2396					2454
	Sn117		1100		1231		1416			1686		1818	1930		2254		2337					2446
Halite	Sn120	873					1413				1762		1938	2214			2324					2474
	Sn121		988	1097			1440				1704	1806	1945	2076	2249		2330					2474
	Sn122	883					1415						1925		2219		2396	2444				2474
	Sn123		979		1200		1448					1801	1943		2219							2474
	Sn124		983		1202		1453					1806	1945					2454				
	Sn125		980		1203		1447					1806	1945									2474
	Sn126		979	1192			1446					1805	1942									2476
	Sn128	877					1415						1927	1985	2254	2335	2408					2474
Thenardite							1427					1665	1957	2082	2128	2263	2339					2453
				1127	1204							1720	1837									

reference spectrum and a test spectrum from two-band data represented on a two-dimensional plot as two points. SAM compares each pixel in the image with every endmember for each class and assigns a value between zero (low resemblance) and one (high resemblance). Small angles between the two spectra indicate high similarity and high angles indicate low similarity. Each vector has a certain length and direction. The length of the vector represents brightness of the pixel while the direction represents the spectral feature of the pixel. Variation in illumination mainly affects changes in length of the vector, while spectral variability between different spectra affects the angle between their corresponding vectors (Kruse et al. 1993). The main advantage of the SAM algorithm is its easy and rapid use and also it is a very powerful classification method because it represses the influence of shadow effects to accentuate the target reflectance characteristics (De Carvalho and Meneses 2000).

The reference spectra for this study are: (1) field spectra; (2) extracted spectra from the ASTER and Landsat 8 images. Halite, gypsum and thenardite endmembers were selected in the images wherever they observed in the field with GPS coordinates. Three image endmembers were put as input spectra in the SAM method.

Results and discussion

In this paper, performance of SAM method applied on ASTER and Landsat 8 images compared for mapping evaporite minerals using reference spectra both from samples and images.

SAM classification using ASTER image

Figure 14 shows SAM classification maps using ASTER images based on two types of spectra. In Fig. 14a, three used spectra were acquired from ASTER images as halite, gypsum and thenardite based on the coordinates that were taken from the field. It should be mentioned that as thenardite is being under surface and also less abundant in the study area, therefore, it was tried to use the acquired spectrum of the image where Na-sulfate mine was reported and observed in the field. In Fig. 14b, the map of SAM classification based on the laboratory spectra is presented. In both maps, Halite consist the central part of the playa and gypsum surrounds it as a narrow strip and it forms a layer in the east and northeastern parts of the playa.

For applying SAM method, the proper angle for each image and for detecting each evaporite mineral was obtained using statistics of the rule image. Based on the field observation and sampling, Eq. 1 was used.

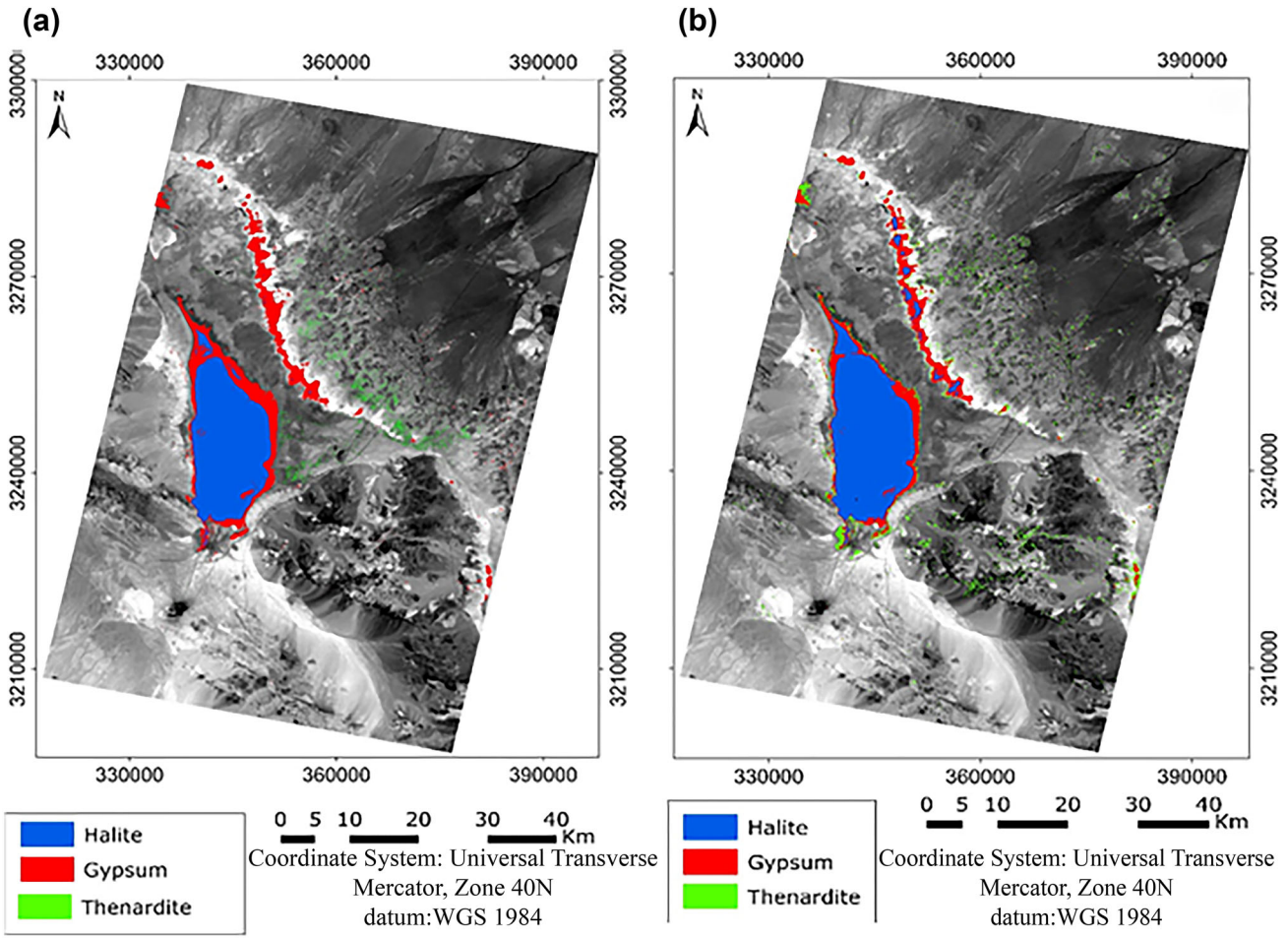

Fig. 14 Evaporate mapping results from SAM method using ASTER images: **a** SAM method using image spectra, **b** SAM method using laboratory spectra

Table 3 Statistics for obtaining proper angles for SAM method using ASTER images

Method	Class	Mean	Standard deviation	Mean-2s (3s)	Angle
SAM method using image spectra	Halite	0.56	0.13	0.31	0.3
	Gypsum	0.29	0.05	0.18	0.17
	Thenardite	0.08	0.11	0.03	0.01
SAM method using laboratory spectra	Halite	0.50	0.12	0.27	0.26
	Gypsum	0.25	0.05	0.14	0.14
	Thenardite	0.17	0.08	0.09	0.09

$$\text{Optimum angle for SAM} = \text{Mean} - X \text{ standard deviation} \quad X = 1 \text{ to } 3 \tag{1}$$

Applied angles for classifying images are presented in Table 3.

The accuracy assessment of the produced maps carried out by conducting map verification using ground truths. In this comparison, two data series were considered, which are training points and sampling points. Accuracy assessment of the map produced by SAM method using ASTER images with image spectra as reference data showed overall accuracy of 91.8% and Kappa Index of 0.87 (Table 4). High accuracy rate made it possible for halite and gypsum to classify just in their own parent class limits, but for thenardite class the result was poor and it is because of its nature of its occurrence. Accuracy assessment results of produced map based on laboratory spectra are presented in Table 4. Based on the laboratory spectra, a map produced with an overall accuracy of 85.96% and a Kappa Index of 0.77 that achieved for halite, gypsum and thenardite (Table 4).

Table 4 Classification accuracy assessment matrix of ASTER images

Reference spectra	Ground truth (%)				
	Class	Halite	Gypsum	Thenardite	Total
Image spectra	Unclassified	0.00	0.00	63.64	8.19
	Halite	100.00	0.00	0.00	47.37
	Gypsum	0.00	100.00	0.00	39.77
	Thenardite	0.00	0.00	36.36	4.68
	Total	100.00	100.00	100.00	100.00
Overall accuracy = 91.81%					
Kappa coefficient = 0.86					
Laboratory Spectra	Unclassified	0.00	0.00	100.00	12.87
	Halite	100.00	2.94	0.00	48.54
	Gypsum	0.00	97.06	0.00	38.60
	Thenardite	0.00	0.00	0.00	0.00
	Total	100.00	100.00	100.00	100.00
Overall accuracy = 85.96%					
Kappa coefficient = 0.77					

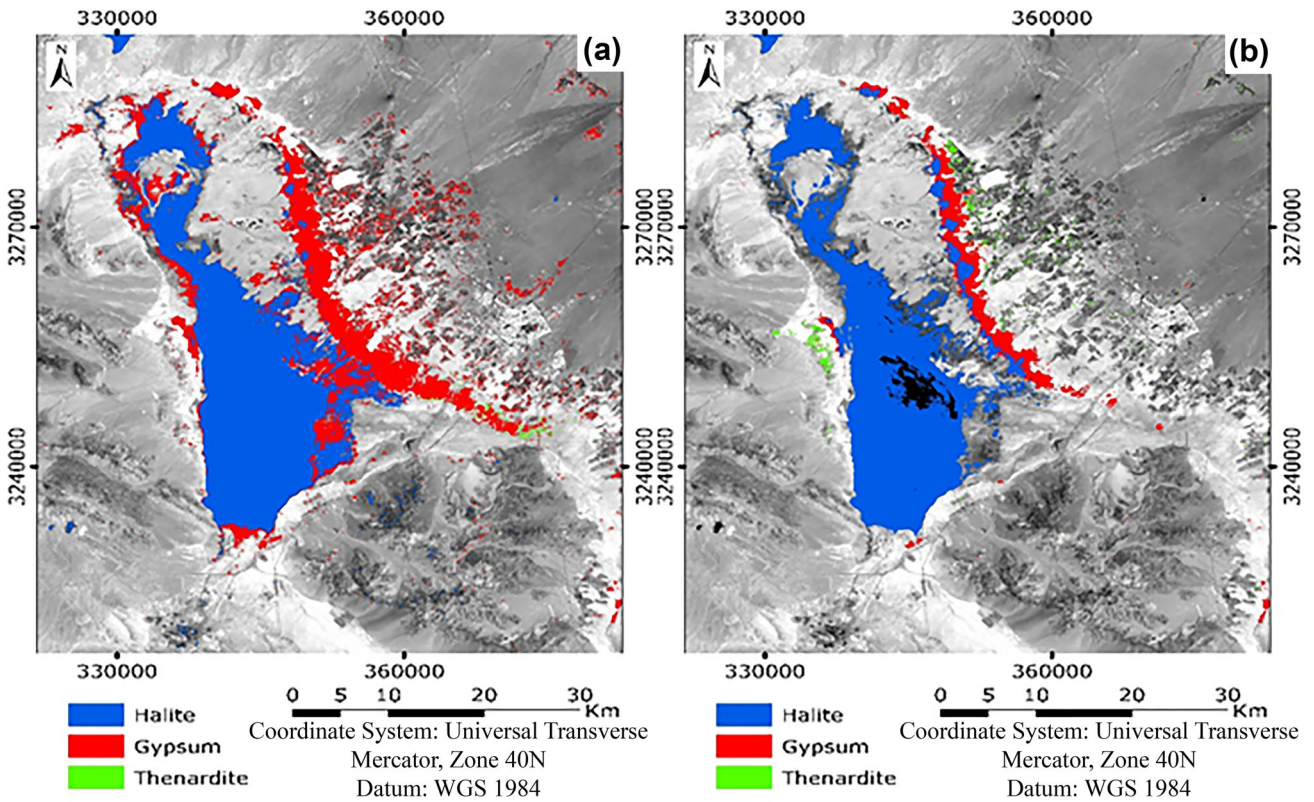

Fig. 15 Evaporate mapping results from SAM method using Landsat 8 image: **a** SAM method using image spectra; **b** SAM method using laboratory spectra

SAM classification using Landsat 8 images

Landsat 8 image for this study was acquired exactly on the sampling day of sampling. SAM classification using image spectra which were acquired from the sampling points shows the distribution of salt pan properly (Fig. 15a). Based on the accuracy assessment results (Table 5), thenardite was detected here better than ASTER image. Figure 15b shows the SAM output classification map created based on laboratory spectra. In the produced map, it can be seen that halite is classified correctly, and gypsum shows almost good result. Applied

Table 5 Statistics for obtaining proper angles in SAM method using Landsat 8 images

Method	Class	Mean	Standard deviation	Mean-2s (1s)	Angle
SAM method using image spectra	Halite	0.34	0.08	0.26 (1s)	0.26
	Gypsum	0.14	0.04	0.10 (1s)	0.103
	Thenardite	0.07	0.06	0.006 (1s)	0.006
SAM method using laboratory spectra	Halite	0.29	0.04	0.20 (2s)	0.2
	Gypsum	0.19	0.05	0.01 (1s)	0.12
	Thenardite	0.19	0.06	0.11 (2s)	0.11

Table 6 Classification accuracy assessment matrix of Landsat 8 images

Reference Spectra	Ground truth (%)				
	Class	Halite	Gypsum	Thenardite	Total
Image spectra	Unclassified	0.00	0.00	37.50	4.72
	Halite	100.00	0.00	0.00	62.60
	Gypsum	0.00	100.00	0.00	24.80
	Thenardite	0.00	0.00	62.50	7.87
	Total	100.00	100.00	100.00	00.00
Overall accuracy = 95.27%					
Kappa coefficient = 0.91					
Laboratory Spectra	Unclassified	0.00	0.00	100.00	12.60
	Halite	28.57	100.00	0.00	69.69
	Gypsum	71.43	0.00	0.00	17.72
	Thenardite	0.00	0.00	0.00	0.00
	Total	100.00	100.00	100.00	100.00
Overall accuracy = 80.31%					
Kappa coefficient = 0.62					

statistics for obtaining proper SAM angles for Landsat8 are presented in Table 5.

Overall accuracy and Kappa coefficient of 95.27% and 0.91 were achieved for SAM classification of Landsat 8 using image spectra. Overall accuracy of 80.31% and Kappa coefficient of 0.62 were obtained for Landsat 8 using sample spectra (Table 6).

Source rocks for Sirjan Playa

Sirjan playa has been formed in a tectonic depression that drains a vast catchment area. Krinsley (1970) divided this playa landform into two geomorphic surfaces as clay flat (68% of the playa surface) and salt crust (32% of the playa surface), but Farpoor et al. (2012) divided the playa landform into five different geomorphic surfaces including non-saline clay flat, saline non-puffy ground clay flat, clay flat with puffy ground, wet zone and salt crust. It is surrounded by mountains that cause its isolation, alluvial fans, and dry and saline mudflats.

Precipitation of evaporite minerals in playas and closed basins demonstrates a zonation. Evaporation and concentration of brine develops this zonation. Less soluble minerals such as carbonates precipitate as first minerals and their highest concentrations occurs in playa margin, whereas highly soluble minerals precipitate in the center of playa. Gypsum is the most abundant sulfate mineral in Sirjan area and thenardite is another sulfate, but its abundance is less. Halite shows increasing trend from margin to the center of the playa.

Water influx into the basins is mainly via ground water discharges, ephemeral rivers and direct precipitation. Nazemzadeh Shoaei and Azizan (1990) based on exploratory drilling and collected core samples reported that there is an impermeable layer under the salt crust that interrupts the connection between groundwater and the surface salt, thus the main feeding water regime in Sirjan playa is surface runoff and the sub-surface runoff originating from surrounding alluvial fans. The playa is almost fed from all directions, but higher soil moisture due to sub-surface runoff originating from alluvial fans located in the northeast of the salt pan (Farpoor et al. 2012; Krinsley 1970) Moving down-slope from mountains towards the playa, soil salinity increases. During the wet months, the ephemeral rivers along with smaller rivulets carry waters with the sediments from the catchment into the playa. Sediments are composed of chemical and clastic minerals and towards the center of the area, chemical minerals

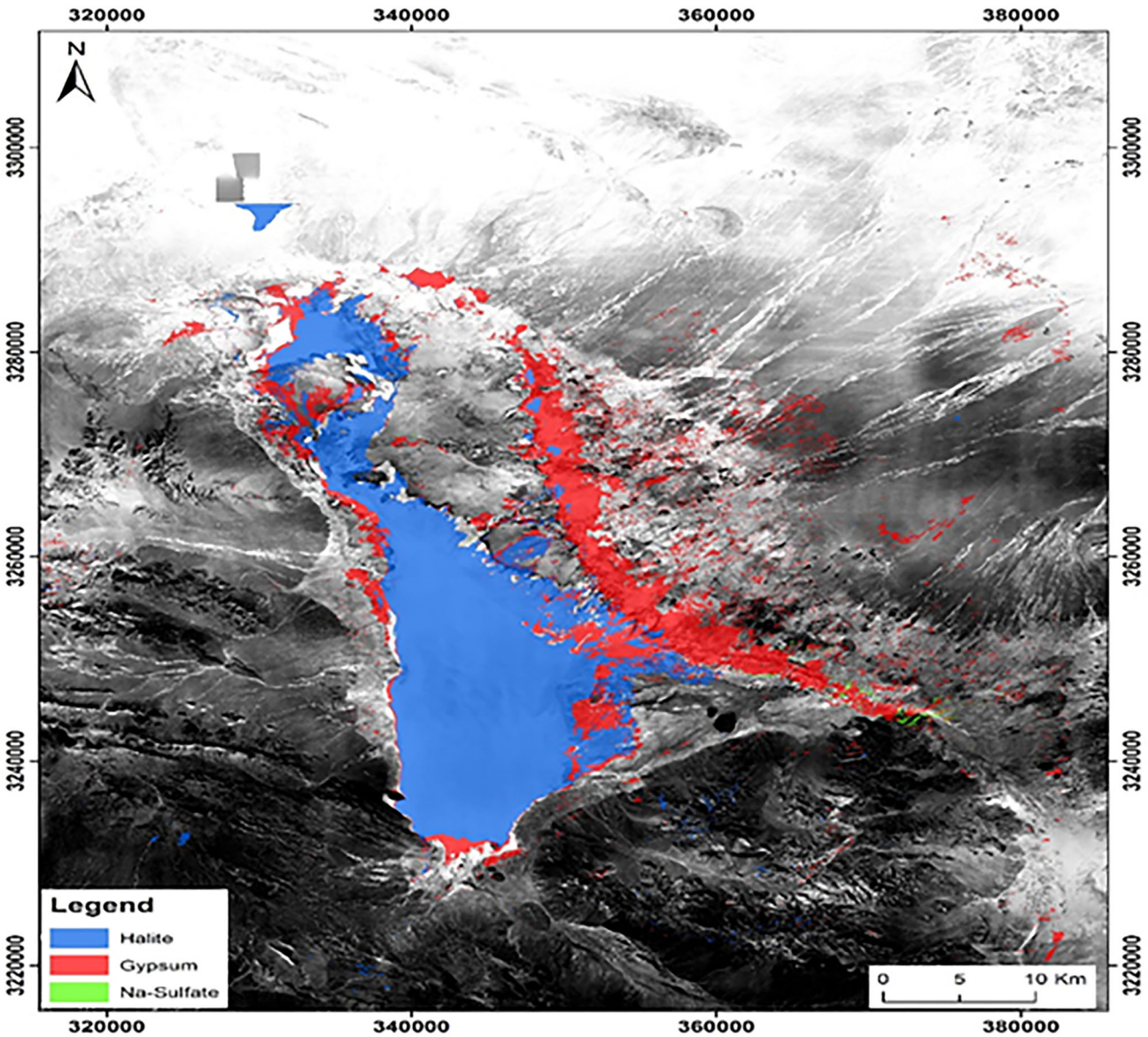

Fig. 16 A mosaic of about 300 aerial photographs which were acquired in October 1956 on which mapped minerals are overlain. As seen from this mosaic of aerial photographs, the feeding drainages are mostly from the north and eastern parts. Coordinate System: Universal Transverse Mercator, Zone 40N. Datum: WGS 1984

(evaporites) dominate, whereas in the marginal areas clastic sediments take over.

As mentioned before, Sirjan playa basin is surrounded by diverse rocks and formations and receives an immense variety of the incoming flow of chemicals. According to the mineralogical composition of several samples of Sirjan pan and based on Eugster and Hardie (1978) models, it can be speculated that composition of the pan water inflows are enriched in Mg + Ca and less HCO_3 and Ca is more than Mg (Nazemzadeh Shoaei and Azizan 1990).

The chemistry of inflowing waters is closely related to the major rock types in the drainage areas and the mode of chemical weathering of rocks and soils. Most of the streams as seen from the mosaicked aerial photographs are flowing into the playa from the northeast and east of the area and in this mosaicked photograph it is clear that the density of alluvial fans and the most feeding part is in the eastern and northeastern parts of the playa that originate from the mountains in Urumieh-Dokhtar volcanic-sedimentary belt (Fig. 16). In addition, for highlighting the most important inflows to the playa, digital elevation model (DEM) of the area and satellite images were used (Fig. 17). Based on what can be seen in Fig. 17, the main feeding drainage system of playa is originated from the northern and eastern mountains and the role of southern and western mountains is less important, therefore, this

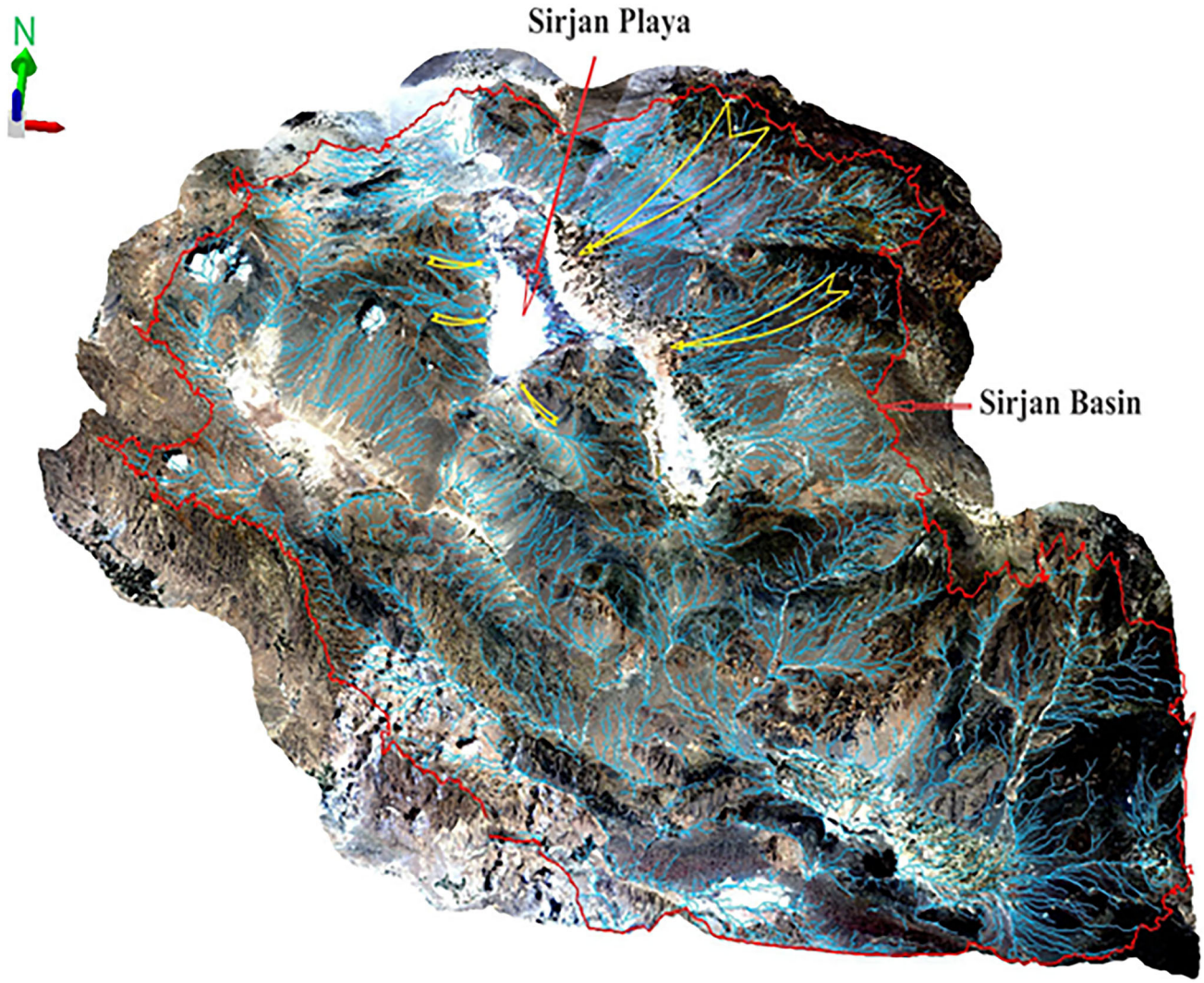

Fig. 17 A general view of the study area. False color composite of bands 4, 3 and 2 of Landsat 8 in *red*, *green* and *blue*, respectively, is overlain on DEM of the area. Drainage systems in the study area are shown in *blue*. *Red line* shows the boundaries of the Sirjan drainage basin

playa receives much of its inflow from north-east and eastern parts of the area (Urumieh-Dokhtar mountains) which is mainly composed of Eocene volcanic formations and sedimentary rocks.

Conclusions

One of the most common strategies for material mapping is the use of similarity measures. In this study, SAM method was applied for mapping evaporite minerals in Sirjan playa. Image classification of ASTER and Landsat 8 images were compared to highlight the best image for mapping evaporite minerals in the study area. Reference spectra for measuring similarity consist of image spectra and laboratory spectra. According to the overall accuracy of classification methods Landsat 8 image using image spectra has the best result with the overall accuracy of 95.27%, whereas ASTER image classification using image spectra as the reference spectra presents the overall accuracy of 91.81%.

Laboratory spectra had a better result with ASTER rather than Landsat and the overall accuracies for these cases are 85.96 and 80.31% for ASTER and Landsat, respectively. It should be mentioned that SAM method for discrimination of evaporite minerals in Sirjan area had very good results based on the achieved accuracies.

Thenardite detection is problematic and the best classification accuracy for this mineral is achieved by Landsat 8 image using image spectra as reference spectra.

Using data such as drainage system of Sirjan basin, digital elevation model, mosaic of old aerial photographs and false color composite image of this area showed that the main source of inflows and sediments to the playa is

from north-east and eastern parts of the playa, where the volcanic and sedimentary rocks of Urumieh-Dokhtar mountains are located.

Acknowledgements We thank the reviewers of the journal for their comments and suggestions that improved the quality of the manuscript. The authors gratefully acknowledge University of Shahid Bahonar of Kerman for providing financial support and field work facilities and Iranian Mines & Mining Industries Development and Renovation (IMIDRO) for financial and technical support of this research. Institute of Science and High Technology and Environmental Sciences in Mahan, Kerman has provided the spectroradiometer for collection of spectra.

References

Alavipanah SK (2000) The use of remote sensing and GIS to detect salt crust in the Iranian deserts. In: Remetey-Fülöpp G, Clevers J, Klaas Beek J (eds) XIXth ISPRS congress, Amsterdam, The Netherlands, 16–23 July 2000. International Society for Photogrametry and Remote Sensing, pp 39–45

Alavipanah SK, Pouyafar AM (2005) Potentials and constraints of soil salinity studies in two different conditions of Iran using Landsat TM data. Paper presented at the 31st international symposium on remote sensing of environment, Saint Petersburg, Russia, 20–24 June

Alavipanah SK, Pouyafar AM, Tahmasebi A (2004a) The application of field soil salinity map in classifying Landsat imagery. In: Goossens R (ed) The 23rd symposium of the European Association of Remote Sensing Laboratories, Ghent, Belgium, 2–5 June 2003, pp 365–369

Alavipanah SK, Komake CB, Ghadiri Masoum M (2004b) Behavior of Landsat Thematic Mapper wavebands on Lut desert (Iran). J Agric Sci Technol 6:31–40

Alavipanah SK, Goossens R, Matinfar HR, Mohammadi H, Ghadiri M, Irannegad H, Alikhah Asl M (2010) The efficiency of Landsat Tm and Etm^{+} thermal data for extracting soil information in arid regions. J Agric Sci Technol 10:439–460

Alavipanah SK, Matinfar HR, Sarmasti N, Jafarbeglou M, Goodarzimehr S (2011) Evaluation of ASTER and LISS III data in identification of saline soils, case study: regions of Iran. In: Geocomputation, London, UK, 20–22 July 2011. University College London, pp 134–146

Berberian M, King GCP (1981) Towards a paleogeography and tectonic evolution of Iran. Can J Earth Sci 18:210–265

Caceres F, Ali-Ammar H, Pirard E (2008) Mapping evaporitic minerals in sud Lipez salt lakes, Bolivia, using remote sensing. Rev Econ Geol 16:199–208

Clark RN, Swayze GA, Gallagher A, King TV, Calvin WM (1993) The U.S. Geological Survey, Digital Spectral Library: Version 1: 0.2 to 3.0 μm. U.S. Geological Survey

Crowley JK (1991) Visible and near-infrared (0.4–2.5 μm) reflectance spectra of Playa evaporite minerals. J Geophys Res 96:16231–16240. doi:10.1029/91jb01714

Crowley JK (1993) Mapping playa evaporite minerals with AVIRIS data: A first report from Death Valley, California. Remote Sens Environ 44:337–356

Csillag F, Pásztor L, Biehl LL (1993) Spectral band selection for the characterization of salinity status of soils. Remote Sens Environ 43:231–242

De Carvalho OA, Meneses PR (2000) Spectral correlation mapper (SCM): an improvement on the spectral angle mapper (SAM). In: 9th JPL airborne earth science workshop, National Aeronautics and Space Administration of US, February 2000. JPL Publication Pasadena, CA

Dimitrijevic MD, Dimitrijevic MN, Djordjevic M, Vulovic D (1971) Geological map of Pariz, sheet no. 7149, 1:100,000 series. Geological Survey of Iran, Tehran, Iran

Drake NA (1995) Reflectance spectra of evaporite minerals (400–2500 nm): applications for remote sensing. Int J Remote Sens 16:2555–2571. doi:10.1080/01431169508954576

Drever JI (1997) The geochemistry of natural waters: surface and groundwater environments, 3rd edn. Prentice Hall, New Jersey

Duda K, Daucsavage J (2015) Advanced spaceborne thermal emission and reflection radiometer (aster) level 1 precision terrain corrected registered at-sensor radiance product (ast_l1t). US Geological Survey, USA

Eugster HP (1980) Geochemistry of evaporitic lacustrine deposits. Annu Rev Earth Planet Sci 8:35–63. doi:10.1146/annurev.ea.08.050180.000343

Eugster HP, Hardie LA (1978) Saline lakes. In: Lerman A (ed) Lakes: chemistry: geology and physics. Springer, New York, pp 237–293. doi:10.1007/978-1-4757-1152-3_8

Farpoor MH, Neyestani M, Eghbal MK, Esfandiarpour Borujeni I (2012) Soil–geomorphology relationships in Sirjan playa, south central Iran. Geomorphology 138:223–230. doi:10.1016/j.geomorph.2011.09.005

Gaffey SJ (1987) Spectral reflectance of carbonate minerals in the visible and near infrared (0.35–2.55 μm). J Geophys Res 92:1429–1440

Hardie LA, Eugster HP (1970) The evolution of closed-basin brines Mineralogical Society of America Special. Publication 3:273–290

Howari FM, Goodell PC, Miyamoto S (2002) Spectral properties of salt crusts formed on saline soils. J Environ Qual 31:1453–1461. doi:10.2134/jeq2002.1453

Hunt GR (1977) Spectral signatures of particulate minerals in the visible and near infrared. Geophysics 42:501–513

Hunt GR, Salisbury JW (1970) Visible and near-infrared spectra of minerals and rocks: I silicate minerals. Mod Geol 1:283–300

Hunt GR, Salisbury JW (1971) Visible and near infrared spectra of minerals and rocks. II. Carbonates Mod Geol 2:23–30

Kavak KS (2005) Recognition of gypsum geohorizons in the Sivas Basin (Turkey) using ASTER and Landsat ETM+ images. Int J Remote Sens 26:4583–4596. doi:10.1080/01431160500185607

Keskin Ş, Şener M, Şener MF, Öztürk MZ (2016) Depositional environment characteristics of Ulukışla Evaporites, *Central Anatolia, Turkey*. Carbonates Evaporites. doi:10.1007/s13146-016-0292-7

Krinsley DB (1970) A geomorphological and paleoclimatological study of the playas of Iran. Ph.D. thesis, Geological Survey of United States

Kruse FA (1988) Use of Airborne Imaging Spectrometer data to map minerals associated with hydrothermally altered rocks in the northern Grapevine Mountains, Nevada and California. Remote Sens Environ 24:31–51. doi:10.1016/0034-4257(88)90004-1

Kruse FA, Lefkoff AB, Boardman JW, Heidebrecht KB, Shapiro AT, Barloon PJ, Goetz AFH (1993) The Spectral image processing system (SIPS) interactive visualization and analysis of imaging spectrometer data. Remote Sens Environ 44:145–163

Landgrebe D (2000) On the relationship between class definition precision and classification accuracy in hyperspectral analysis. In: geoscience and remote sensing symposium, 24–28 July 2000. IEEE, pp 147–149

Matinfar HR, Alavipanah SK, Zand F, Khodaei K (2011) Detection of soil salinity changes and mapping land cover types based upon remotely sensed data. Arab J Geosci 6:913–919. doi:10.1007/s12517-011-0384-6

Miralles DG, Holmes TRH, De Jeu RAM, Gash JH, Meesters AGCA, Dolman AJ (2011) Global land-surface evaporation estimated from satellite-based observations. Hydrol Earth Syst Sci 15:453–469

Mougenot B, Pouget M, Epema GF (1993) Remote sensing of salt affected soils. Remote Sens Rev 7:241–259. doi:10.1080/02757259309532180

Nazemzadeh Shoaei M, Azizan H (1990) Preliminary exploration of potash in Sirjan Playa. Geological survey of Iran, Management of the southeastern Region (Kerman branch)

Nazemzadeh Shoaei M, Roshan Ravan J, Azizan H (1996) Geological map of Baghat, sheet no. 7147, 1:100,000 series. Geological Survey of Iran, Kerman, Iran

Öztan NS (2008) Evaporate mapping in Bala region (Ankara) by remote sensing techniques. M.Sc. Thesis, Middle East Technical University

Öztan NS, Süzen ML (2011) Mapping evaporate minerals by ASTER. Int J Remote Sens 32:1651–1673. doi:10.1080/01431160903586799

Özyavaş A (2016) Assessment of image processing techniques and ASTER SWIR data for the delineation of evaporates and carbonate outcrops along the Salt Lake Fault, Turkey. Int J Remote Sens 37:770–781. doi:10.1080/2150704X.2015.1130873

Pakzad HR, Ajalloeian R (2004) Geochemistry of the Gavkhoni playa lake brine. Carbonates Evaporites 19:67–74. doi:10.1007/BF03175196

Perkins T, Adler-Golden S, Matthew M, Berk A, Anderson G, Gardner J, Felde G (2005) Retrieval of atmospheric properties from hyper and multispectral imagery with the FLAASH atmospheric correction algorithm. In: International Society for Optics and Photonics, pp 1–11. doi:10.1117/12.626526

Reeves CC (1978) Economic significance of playa lake deposits. In: Matter A, Tucker ME (eds) Modern and ancient lake sediments. Blackwell Publishing Ltd., Oxford, pp 279–290. doi:10.1002/9781444303698.ch15

Roshan Ravan J, Eshraghi SA, Sabzehei M (1996) Geological map of Sirjan, sheet no.7148, 1:100,000 series. Geological survey of Iran, Kerman, Iran

Ross SD (1974) Sulphates and other oxy-anions of Group VI. In: Farmer VC (ed) The infrared spectra of minerals. Mineralogical Society, London, pp 423–444. doi:10.1180/mono-4

Roy PD, Smykatz-Kloss W (2007) REE geochemistry of the recent playa sediments from the Thar Desert, India: an implication to playa sediment provenance. Chem Erde 67:55–68. doi:10.1016/j.chemer.2005.01.006

Sabzehei M, Eshraghi SA, Roshan Ravan J, Seraj M (1997) Geological map of Gole-Gohar, sheet no. 7048, 1:100,000 series. Geological survey of Iran, Kerman, Iran

Salisbury JW (1991) Infrared (2.1–25 μm) spectra of minerals. Johns Hopkins University Press, Baltimore, p 267

Shahabpour J (2005) Tectonic evolution of the orogenic belt in the region located between Kerman and Neyriz. J Asian Earth Sci 24:405–417. doi:10.1016/j.jseaes.2003.11.007

Sheikholeslami MR (2015) Deformations of Palaeozoic and Mesozoic rocks in southern Sirjan, Sanandaj-Sirjan Zone, Iran. J Asian Earth Sci 106:130–149

Sracek O, Veselovský F, Kříbek B, Malec J, Jehlička J (2010) Geochemistry, mineralogy and environmental impact of precipitated efflorescent salts at the Kabwe Cu–Co chemical leaching plant in Zambia. Appl Geochem 25:1815–1824. doi:10.1016/j.apgeochem.2010.09.008

Stocklin J (1968) Structural history and tectonics of Iran: a review. AAPG Bull 52:1229–1258

Vane G, Goetz AFH (1988) Terrestrial imaging spectroscopy. Remote Sens Environ 24:1–29

Warren JK (2006) Evaporites: sediments, resources and hydrocarbons. Springer, Berlin

Warren JK (2010) Evaporites through time: tectonic, climatic and eustatic controls in marine and nonmarine deposits. Earth Sci Rev 98:217–268. doi:10.1016/j.earscirev.2009.11.004

Zehtabian GR, Alavipanah SK, Ehsani AH (2002) The use of Landsat Thematic Mapper data for mapping the marginal playa soils in Damghan playa, Iran. Paper presented at the spatial information in mapping and cadastral systems, Washington, DC, USA, 19–26 April